Russian Geology and Geophysics © 2019, V.S. Sobolev IGM, Siberian Branch of the RAS
Vol. 60, No. 8, pp. 845–861, 2019 *DOI:10.15372/RGG2019069* *Geologiya i Geofizika*

The Oortsog Peridotite–Troctolite–Gabbro Intrusion, Western Mongolia: New Petrological and Geochronological Constraints

M.O. Shapovalova [a,b,] ✉, N.D. Tolstykh [a], R.A. Shelepaev [a,b], L.V. Tsibizov [c]

[a] *V.S. Sobolev Institute of Geology and Mineralogy, Siberian Branch of the Russian Academy of Sciences, pr. Akademika Koptyuga 3, Novosibirsk, 630090, Russia*

[b] *Novosibirsk State University, ul. Pirogova 2, Novosibirsk, 630090, Russia*

[c] *A.A. Trofimuk Institute of Petroleum Geology and Geophysics, Siberian Branch of the Russian Academy of Sciences, pr. Akademika Koptyuga 3, Novosibirsk, 630090, Russia*

Received 28 February 2018; received in revised form 14 December 2018; accepted 5 February 2019

Abstract—New petrological, isotope-geochronological, and geophysical data reveal two phases of magmatism in the Oortsog mafic–ultramafic intrusion in Western Mongolia. The intrusion consists of (i) rhythmically layered peridotite gabbro (278.7 ± 2.5 Ma) and (ii) poorly differentiated biotite-containing amphibole–olivine gabbro and gabbronorite (272 ± 2 Ma). The inverse upward succession from leucocratic to melanocratic lithologies within each rhythm indicates that the intrusion was tectonically overturned. The earlier rocks (phase 1) have lower contents of major oxides ($Na_2O + K_2O$, TiO_2, and P_2O_5) than the later ones (phase 2) and show different patterns of incompatible elements. The intrusive rocks of phases 1 and 2 were derived from depleted (positive ε_{Nd}) and enriched (negative ε_{Nd}) mantle sources, respectively. The calculated parental melts of both phases belong to picritic (Mg-rich) basaltic magma. More insight into the intrusion structure was gained by mapping magnetic anomalies.

Keywords: mafic–ultramafic rocks, layered intrusion, Permian age, magnetic-flux density anomaly, Western Mongolia

INTRODUCTION

Differentiated and layered mafic–ultramafic intrusions with sulfide mineralization in Southeastern Siberia (Kislov, 1998; Polyakov et al., 2013; Podlipsky et al., 2015), Vietnam (Svetlitskaya et al., 2015), China (Luo et al., 2014), and Mongolia (Izokh et al., 1998) have received much recent attention. Studies of these mantle-derived intrusions provide an important contribution to petrological theories and make basis for reconstructing the history of geological structures.

The Central Asian orogenic belt (CAOB) accommodates numerous peridotite–pyroxenite–anorthosite–gabbronorite intrusions which have no spatial relation to regional faults or ophiolites (Izokh et al., 1990). Intrusions in the Hangayn Mountains belong to the Early Paleozoic Tamir complex consisting of the Ider, Baidarik, and Tamir fields (Polyakov et al., 1984). Mafic rocks, including the Oortsog and Dulaan intrusions from the Tamir complex, were related to the Tarim plume (Mao et al., 2018). The Tamir field comprises the Oortsog intrusion with sulfide (Izokh et al., 1990) and PGE (Shapovalova et al., 2016) mineralization and the Dulaan Intrusion cropping out 1.5 km apart, with disseminated sulfide mineralization; both intrusions store economic Cu–Ni–PGE deposits (Mao et al., 2018). The Oortsog intrusion formed in two events (Shapovalova et al., 2016) from melts fractionated to different degrees. The objectives of this study include detecting the features of magmatic phases in the Oortsog intrusion in Western Mongolia from petrography, mineralogy, and major- and trace-element chemistry of rocks; timing the two intrusion phases; and reconstructing the intrusion history in a petrological model. The results will provide insights into the origin and evolution of basaltic magmas, as a subject of basic petrological research, and will allow relating the events that produced the Oortsog intrusion to a specific stage in the CAOB history.

GEOLOGICAL SETTING

The Oortsog intrusion is located north of the Main Mongolian Lineament in the center of the Central Asian Orogenic Belt that borders the Siberian craton in the north and the Tarim and North China cratons in the south. The northern and southern CAOB segments are, respectively, Early Paleozoic (500–400 Ma) and Middle Paleozoic (400–230 Ma) orogens (Yanshin, 1974; Dergunov et al., 1980).

The territory of Mongolia is an intricate collage of terranes (Badarch et al., 2002; Tomurtogoo, 2002), with a relatively small Precambrian block of Hangayn in the center, surrounded with several accreted terranes that formed in different tectonic settings. Therefore, the setting of the mag-

✉ Corresponding author.
E-mail adress: shapovalovam@igm.nsc.ru (M.O. Shapovalova)

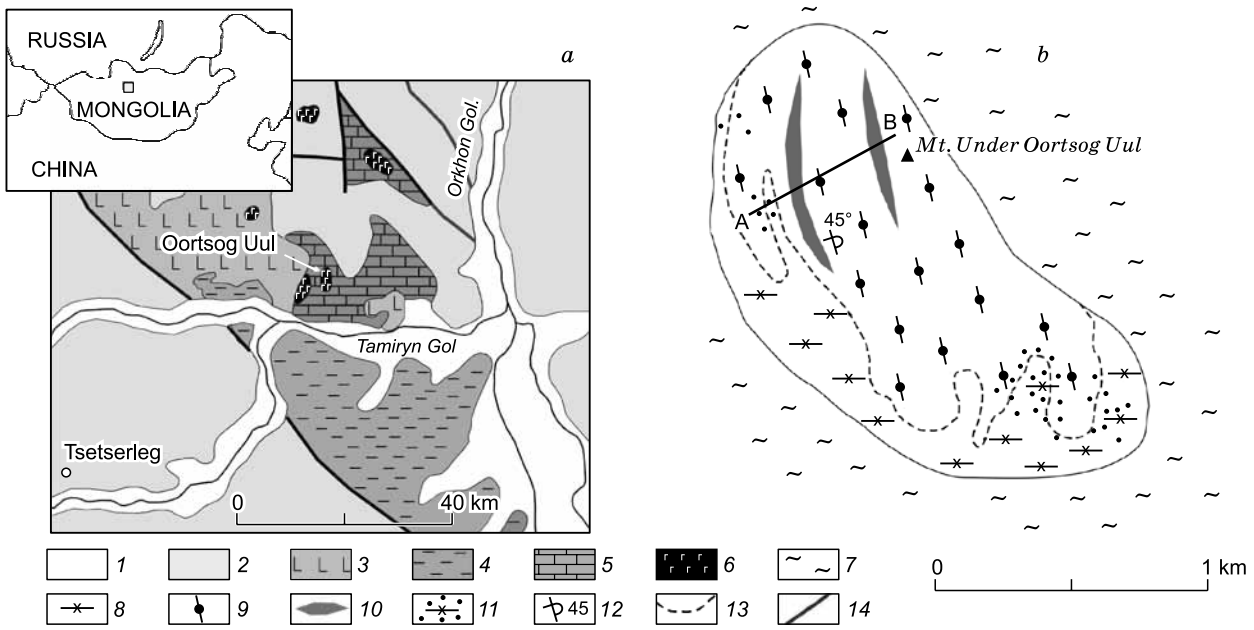

Fig. 1. Geological map of the northern slope of the Hangayn Range (Yanshin et al., 1989) (*a*) and the Oortsog intrusion (our data) (*b*). *1*, Quaternary sediments; *2*, clastic sediments (PZ_3–MZ_2); *3*, basalt (PZ_3); *4*, green schist (R_3–$Є_1$); *5*, carbonate rocks (R_3–$Є_1$); *6*, intrusions of Tamir complex (PZ_1); *7*, schist and gneiss; *8*, phase 2 gabbro and gabbronorite; *9*, *10*, phase 1 rocks: olivine gabbro, gabbronorite and troctolite (*9*), ultramafics (plagioharzburgite, lherzolite) and melanotroctolite (*10*); *11*, gabbro with disseminated sulfide mineralization; *12*, overturned bedding; *13*, contact between two intrusion phases; *14*, faults.

matic activity remains controversial and has been explained in two main models: (1) two volcanoplutonic belts in the active margin of the Mongolia–Siberia continent (Gordienko, 1987; Ernst, 2014, 2016) and (2) the Mongolian hotspot (Kuzmin et al., 2010; Yarmoluk and Kuzmin, 2012) that existed in the Late Permian–Early Triassic (Kuzmin and Yarmoluk, 2014). The Oortsog peridotite–gabbro layered intrusion is exposed over ~5 km^2 on the northern slope of the Hangayn Mountains in the left side of the Tamiryn-Gol River (Fig. 1*a*). It intrudes Proterozoic metamorphic rocks (quartzite, gneiss, and amphibolite), and the contact is marked by traces of melting in the northwestern part of the intrusion. The central part spatially coincides with the top of Under Oortsog Uul Mountain at 1740 m asl (Fig. 1*b*). The Oortsog and other gabbroic intrusions imaged in the 1:200 000 map were previously interpreted as resulting from an Early Paleozoic magmatic event (Khosbayar et al., 1987). The study area also includes widespread Permian mafic–ultramafic and gabbro–monzodiorite rocks of the Selenga complex.

METHODS

Whole-rock major-element chemistry (56 samples) was analyzed by the X-ray Fluorescence (XRF) method at the Analytical Center for Multielement and Isotope Studies (Novosibirsk) on a Thermo Scientific *ARL 9900* spectrometer (Switzerland), with a detection limit of 30 ppm. Trace elements were determined in 28 samples by inductively coupled plasma mass spectrometry (ICP-MS) on a Finnigan *MAT Element-I* mass spectrometer (Germany) at the V.S. Sobolev Institute of Geology and Mineralogy (IGM, Novosibirsk), following the procedure from (Nikolaeva et al., 2008). Minerals were identified by WDS X-ray spectrometry (121 analyses) on a Jeol *JXA-8100* microanalyzer (Japan). The data were calibrated using domestic standards. The operation conditions were E_0 = 20 kV, I = 40 nA, t = 10 s.

The samples were dated by the SHRIMP-II U–Pb method on zircons on an ASI Sensitive High Resolution Ion MicroProbe II, SIMS (Australia), at the Center for Isotope Studies of the A.P. Karpinsky Russian Geological Research Institute (VSEGEI, St. Petersburg). ^{39}Ar–^{40}Ar dating was performed on biotite and amphibole monofractions at IGM (Novosibirsk) on a GV-Instruments *Argus* multicollector mass spectrometer (Great Britain).

The Sm–Nd systematics were studied by thermal ionization mass spectrometry (TIMS) on a *ThermoFinnigan Triton* analyzer, to an accuracy of <0.001% at the Geological Institute, Kola Science Center (Apatity). The Sm/Nd measurements followed the procedure described by Zhuravlev et al. (1987).

The parent melt compositions for the Oortsog rocks were reconstructed by modeling with the *COMAGMAT 3.57* software (Ariskin et al., 1993) for layered intrusions. The input parameters were: a pressure of 2 kbar and an oxygen fugacity at the QFM (quartz–fayalite–magnetite) buffer.

The field studies of the Oortsog intrusion included ground-based magnetic survey for mapping anomalies of the magnetic field (see the respective section below for method details).

RESULTS

Petrography

The Oortsog intrusion emplaced in two events (Shapovalova et al., 2015) that produced (1) rhythmically layered biotite-free peridotite–troctolite–gabbronorite and (2) biotite-bearing amphibole– olivine gabbro with low-variable percentages of the melanocratic component (Fig. 1*b*). The two phases show a sharp contact in the southern part of the intrusion, with sulfide mineralization along the contact (Shapovalova et al., 2017). Our new results have provided updates to the previously published model of the intrusion (Izokh et al., 1990).

The rocks of two phases differ in petrography and mineralogy. Those of **phase 1** split into four groups according to the contents of the leucocratic component:

Ultramafics: plagioharzburgite and lherzolite that crop out as lens-like bodies in the northern part of the intrusion and have hypidiomorphic (locally poikilitic) textures. Plagioharzburgite consists of olivine (70–85 vol.%), plagioclase (5 vol.%), and orthopyroxene (10–25 vol.%). The mineralogy of lherzolite includes olivine (70 vol.%), plagioclase (0–5 vol.%), orthopyroxene (10–15 vol.%), and clinopyroxene (10–15 vol.%) corresponding to diopside and augite (Mg# = 73–88%).

Subultramafics: troctolite (60 vol.% Ol, 25 vol.% Pl, 10–15 vol.% Cpx + Opx) and melanocratic olivine gabbro and gabbronorite (60–80 vol.% Ol, 10–30 vol.% Pl, 10–15 vol.% Cpx; 60–80 vol.% Ol, 10–30 vol.% Pl, 10–15 vol.% Cpx + Opx) in the upper parts of rhythms.

Mafics: olivine gabbro (5–60 vol.% Ol, 10–80 vol.% Pl, 10–40 vol.% Cpx), among which mesocratic varieties are the most widespread (Fig. 2*a*, *b*), leucogabbro (0–5 vol.%

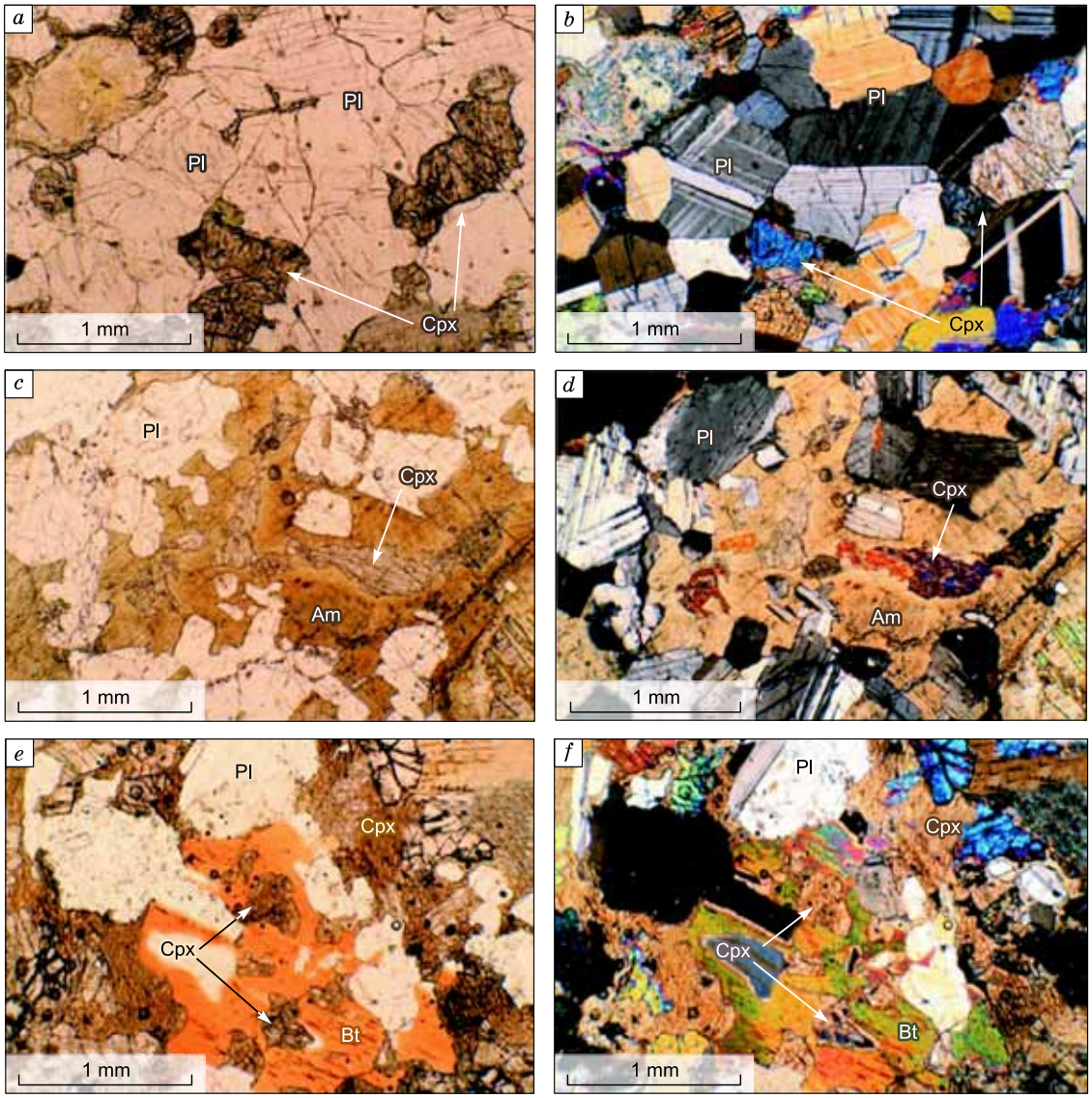

Fig. 2. Mezocratic olivine gabbro, phase 1 (sample Ch-29-14), with gabbroic texture (*a*, *b*); biotite-bearing amphibole mesogabbro, phase 2 (sample V-13061), with poikilitic texture (*c*, *d*); amphibole-olivine mesogabbro, phase 2 (sample Ch-22-14), with poikilitic texture (*e*, *f*). Pl, plagioclase; Cpx, clinopyroxene; Am, amphibole; Bt, biotite. Transmitted light, ppl (*a*, *c*, *e*) and transmitted light, xpl (*b*, *d*, *f*).

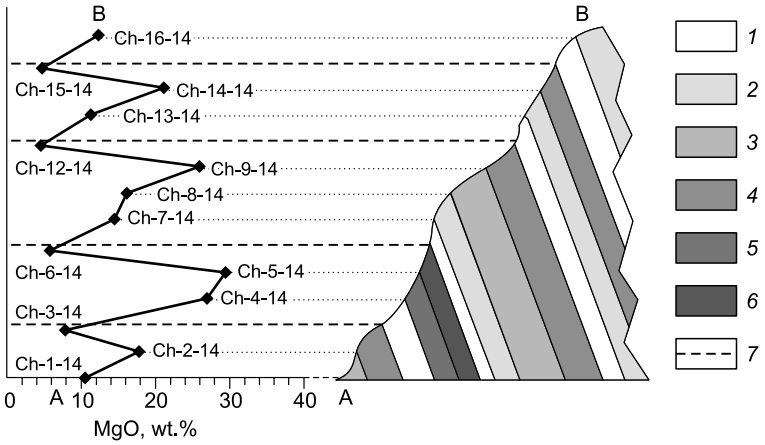

Fig. 3. Cross section along line A–B (Fig. 1*b*) and upsection MgO variations in phase 1 rocks: *1*, olivine leucogabbro; *2*, olivine mesogabbro; *3*, olivine mesogabbronorite; *4*, olivine melanogabbro; *5*, troctolite; *6*, plagioclase peridotite; *7*, boundaries between rhythms.

Ol, 70–90 vol.% Pl, 10–30 vol.% Cpx), and hornblende gabbro (5–30 vol.% Ol, 50–70 vol.% Pl, 10–30 vol.% Cpx, 5–10 vol.% Hbl) identified according to magnesian hornblende (77.3–94.9% Mg#, 0.6–0.2% ^{IV}Al, 0.08–0.04% Ti).

Anorthosite: anorthosite with 90 vol.% calcic plagioclase ($An_{65–90}$). Anorthosite occurs in the lower part of the intrusion (in its present position); it shows an allotriomorphic texture and the greatest alteration degree.

Phase 2 consists of olivine gabbronorite and olivine gabbro (mesogabbro) with minor percentages of plagioclase and, hence, a low differentiation degree. Unlike the rocks of phase 1, gabbro of phase 2 contain up to 10 vol.% biotite (Fig. 2*c*, *d*) and 30 vol.% amphibole (Fig. 2*e*, *f*).

Phase 1 rocks retain primary magmatic layering produced by alternation of the four rock groups. Each rhythm begins with ultramafic or mafic rocks and ends with leucocratic varieties. The cross section displays an inverse succession of rocks within each rhythm, with leucocratic rocks below and melanocratic gabbro above (Fig. 3), which may result from tectonic disturbance.

Rock-forming minerals of the Oortsog intrusion

Olivine is a rock-forming mineral in both phases. It reaches 75 vol.% in lherzolite and plagioharzburgite and the content decreases with increasing leucocratic component to zero in leucogabbro, hornblende gabbro, and anorthosite. It is commonly more euhedral than other minerals and partly serpentinized, with reticulate textures, in most cases; the crystal sizes reach 3 mm. It has a chrysolite composition with $Fo_{63–83}$ in phase 1 (Izokh et al., 1990) and $Fo_{73–82}$ in phase 2 (Fig. 4*a*; Table 1). Olivine grains in gabbronorite of phase 1 host <0.25 mm inclusions of green spinel (hercynite). Olivine in phase 2 has orthopyroxene and clinopyroxene rims.

Plagioclase is the most widespread mineral, which is present in all rocks of the intrusion but in different amounts (from 5 vol.% in plagioperidotite to almost 100 vol.% in anorthosite). The An component in the analyzed plagioclases is from An_{75} to An_{98} for phase 1 and from An_{77} to An_{96} for phase 2 rocks, which corresponds to anorthite and bytownite (Fig. 4*b*, Table 2). Plagioclase occurs as anhedral

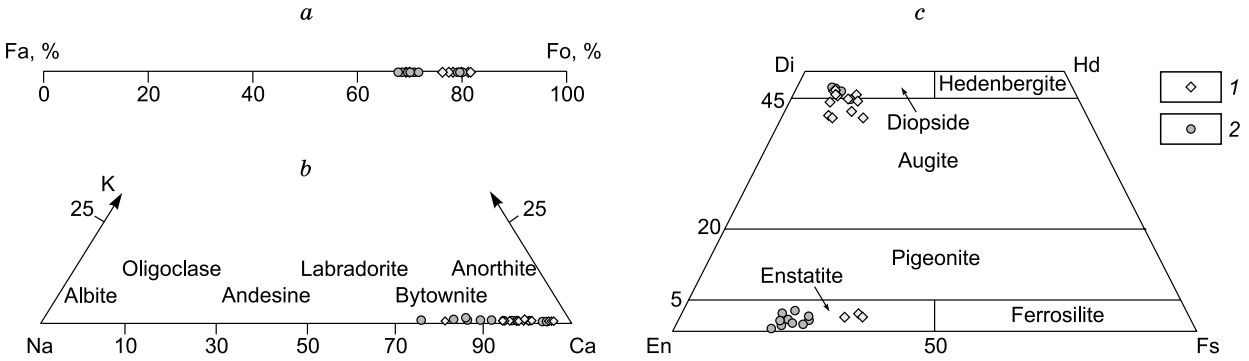

Fig. 4. Compositions of rock-forming minerals from phases 1 (*1*) and 2 (*2*) of the Oortsog intrusion: *a*, olivine; *b*, plagioclase; *c*, pyroxene. Classification of pyroxenes according to (Morimoto, 1989).

Table 1. Mineral chemistry of olivine (wt.%) from Oortsog rocks

Lithology	SiO_2	TiO_2	Cr_2O_3	MnO	FeO	MgO	CaO	Na_2O	K_2O	NiO	Total	Fo, %
Phase 1												
Ol melanogabbro	38.02	bdl	bdl	0.36	22.44	39.83	bdl	0.03	–	0.02	100.70	75.7
	38.61	bdl	bdl	0.34	21.84	40.21	bdl	0.03	–	0.01	101.04	76.4
Ol mesogabbro	39.51	bdl	bdl	0.32	17.67	43.34	bdl	0.02	–	0.05	100.92	81.1
	39.07	bdl	bdl	0.28	19.12	42.36	0.01	0.02	–	0.01	100.86	79.6
Troctolite	39.10	bdl	bdl	0.27	16.48	43.78	bdl	0.03	–	0.08	99.75	82.3
	39.72	bdl	bdl	0.23	15.56	44.61	bdl	0.04	–	0.09	100.25	83.4
Phase 2												
Ol melanogabbro	38.18	0.01	0.02	0.37	21.09	39.55	0.01	0.02	0.02	–	99.26	76.7
	38.62	0.02	0.03	0.31	16.88	43.24	0.02	0.02	0.01	–	99.15	81.8
	39.25	0.02	0.02	0.32	16.69	43.49	0.02	0.02	0.01	–	99.84	82.0
Ol mesogabbro	38.62	0.01	bdl	0.30	21.39	38.83	0.02	bdl	0.00	–	99.16	76.1
	38.43	bdl	bdl	0.32	21.80	39.01	0.04	bdl	bdl	–	99.6	75.9
	38.38	0.01	0.02	0.27	24.17	37.60	0.02	bdl	bdl	–	100.46	73.3
	38.52	0.01	0.01	0.27	24.31	37.89	bdl	bdl	0.01	–	101.02	73.3
	37.88	0.01	0.03	0.24	21.63	39.70	0.01	0.03	0.01	–	99.52	76.4

Note. bdl means below detection limit; em dash means no data. X-ray analysis of rock-forming minerals was performed on a JXA-8100 analyzer at IGM (Novosibirsk), analyst O.S. Khmelnikova.

Table 2. Mineral chemistry of plagioclase (wt.%) from Oortsog rocks

Lithology	SiO_2	Al_2O_3	CaO	Na_2O	K_2O	Total	An, %
Phase 1							
Peridotite	49.42	32.44	15.56	2.73	0.01	100.26	75.85
	45.44	34.57	18.61	0.98	0.01	99.79	91.30
Ol melanogabbro	45.89	34.75	18.59	0.92	0.01	100.45	91.68
	46.03	34.27	18.52	1.05	0.01	100.11	90.64
	44.95	33.89	18.74	0.89	bdl	98.83	92.10
	46.54	33.88	17.87	1.34	bdl	99.88	88.03
Ol mesogabbro	45.62	34.27	16.94	1.32	0.15	98.58	86.83
	43.77	34.75	19.45	0.41	bdl	98.56	96.31
	44.25	35.32	19.31	0.51	bdl	99.55	95.48
Troctolite	45.44	34.45	18.36	1.03	bdl	99.67	90.76
	45.16	34.55	18.55	1.01	0.06	99.58	90.72
Phase 2							
Ol melanogabbro	45.70	34.20	18.62	1.13	0.03	100.04	89.97
	45.25	34.58	18.83	0.95	0.02	99.86	91.52
	44.73	34.99	19.33	0.69	0.02	99.96	93.84
Ol mesogabbro	45.27	34.24	17.32	1.54	0.01	98.62	86.10
	46.66	33.38	15.61	2.10	0.11	99.17	79.90
	47.49	32.24	15.41	2.42	0.05	98.04	77.66
	45.00	34.81	17.99	0.45	bdl	98.24	95.69

Note. TiO_2, Cr_2O_3, MnO, FeO, and MgO contents are below detection.

grains in ultramafic rocks and as laths in leuco- and mesocratic gabbro of phase 2; the laths produce a poikilophitic texture with pyroxene and amphibole oikocrysts. In some cases, plagioclase is replaced by saussurite, more often in anorthosite than in gabbro.

Orthopyroxene occurs as ≤2 mm round prismatic crystals, often irregularly shaped and anhedral relative to olivine. It corresponds to enstatite according to Mg# in the Mg–Fe diagram (Morimoto, 1989), in both phase 1 and 2 rocks (Fig. 4*c*, Table 3).

Table 3. Mineral chemistry of orthopyroxene (wt.%) from Oortsog rocks

Lithology	SiO_2	TiO_2	Al_2O_3	Cr_2O_3	MnO	FeO	MgO	CaO	Na_2O	K_2O	Total	Mg#, %
Phase 1												
Peridotite	53.14	0.13	3.78	0.08	0.38	18.38	18.42	3.28	0.34	0.05	97.96	64.10
Ol mesogabbro	39.90	0.26	14.58	0.11	12.26	0.15	15.03	11.53	1.48	0.13	95.42	68.60
	55.22	0.05	0.96	0.01	18.79	0.49	21.73	1.51	0.11	0.01	98.88	67.33
Troctolite	48.81	1.29	6.19	bdl	13.25	0.30	15.45	11.36	0.99	0.58	98.21	67.51
Phase 2												
Ol melanogabbro	55.44	bdl	1.55	bdl	0.08	12.29	29.37	0.22	bdl	bdl	98.95	80.98
	52.04	0.20	2.07	0.15	0.29	16.60	26.31	1.14	0.08	0.03	98.90	73.85
	53.27	0.19	2.00	0.10	0.29	14.67	28.08	1.29	0.03	0.01	99.95	77.33
Ol mesogabbro	52.83	0.43	1.37	0.11	0.37	18.40	23.00	2.08	0.16	0.08	98.82	69.02
	54.49	0.20	1.17	0.16	0.33	15.88	27.16	0.66	0.01	bdl	100.06	75.30
	53.96	0.17	0.94	0.06	0.32	16.48	26.74	1.01	0.03	0.01	99.72	74.30
	54.18	0.31	1.53	0.09	0.31	13.90	28.27	1.16	0.04	bdl	99.79	78.37
	55.07	0.03	1.51	0.12	0.30	13.52	29.06	0.50	bdl	bdl	100.10	79.30

Table 4. Mineral chemistry clinopyroxene (wt.%) from Oortsog rocks

Lithology	SiO_2	TiO_2	Al_2O_3	Cr_2O_3	MnO	FeO	MgO	CaO	Na_2O	K_2O	Total	Mg#, %
Phase 1												
Peridotite	50.40	0.36	5.19	1.10	4.34	0.11	15.36	22.67	0.31	bdl	99.84	86.31
	51.88	0.42	3.47	0.80	4.75	0.15	16.17	22.38	0.30	bdl	100.30	85.85
	51.89	0.33	3.53	0.95	4.13	0.11	16.41	22.78	0.25	bdl	100.37	87.62
Ol melanogabbro	52.98	0.25	2.40	0.20	6.36	0.19	16.31	21.26	0.23	bdl	100.18	82.05
	52.62	0.40	2.88	0.15	6.68	0.21	15.01	22.70	0.21	bdl	100.85	80.02
	52.19	0.30	2.31	0.11	5.04	0.14	16.07	23.40	0.15	bdl	99.70	85.03
Ol mesogabbro	52.80	0.28	2.19	0.07	5.30	0.17	15.97	23.39	0.16	bdl	100.34	84.30
	51.49	0.54	2.44	0.11	7.89	0.19	14.47	22.33	0.20	0.02	99.67	76.57
	51.01	1.47	2.18	0.09	9.51	0.31	14.52	20.41	0.23	0.01	99.75	73.12
Troctolite	51.56	0.37	3.53	0.83	3.87	0.13	16.39	22.91	0.23	bdl	99.81	88.30
	49.76	0.30	4.32	1.84	5.31	0.10	16.98	21.09	0.17	bdl	99.87	85.07
Phase 2												
Ol melanogabbro	52.83	0.51	2.59	0.11	0.20	5.34	16.15	22.92	0.28	0.02	100.94	84.35
	50.78	0.33	3.42	0.84	0.14	4.92	16.08	21.92	0.19	0.02	98.63	85.35
	51.42	0.56	3.05	0.43	0.19	6.63	15.88	21.05	0.29	0.01	99.50	81.02
Ol mesogabbro	52.16	0.45	2.31	0.27	0.16	5.85	15.59	22.51	0.28	0.01	99.60	82.61
	51.81	0.40	3.67	0.97	0.15	4.55	15.98	21.39	0.49	0.05	99.45	86.22
	52.23	0.35	2.68	0.68	0.15	4.37	15.89	22.53	0.39	0.02	99.29	86.63

Clinopyroxene is common to rocks of both phases and is present in different amounts in all rock groups. Its round grains (within 2 mm) are overgrown with hornblende producing a corona texture; some crystals are within 0.5 mm and have round or platy shapes. Clinopyroxene with enclosed Pl and Opx has a poikilitic texture. In phase 1 rocks, it forms rims around orthopyroxene or olivine. Clinopyroxene has a composition of diopside and augite (Mg# = 73–88%) in phase 1 rocks and diopside (Mg# = 78–86%) in those of phase 2 (Fig. 4*b*, Table 4) (Morimoto, 1989).

Amphibole forms rims around pyroxene (Cpx and Opx) grains or replaces them totally. It is a typical rock-forming mineral in phase 2 samples, where it commonly occurs as ≤3 mm anhedral crystals pleochroic from pale green to brownish-green. Sometimes it is found as oikocrysts in a poikilitic texture (Fig. 2*d*, *e*). Amphiboles in rocks of both phases are most often Mg hornblende (Mg# = 77–95%; 0.6–0.2 ^{IV}Al; 0.08–0.04 Ti). Actinolite and tremolite grains (Table 5) were found in phase 1 rocks where amphibole replaces pyroxenes. Rocks of phase 2 bear pargasite and tchermakite grains, according to the nomenclature of Leake et al. (1997) (Table 6).

Biotite is restricted to rocks of phase 2 and crystallizes as ≤1.5 mm flakes, with biotite-like pleochroism from straw

Table 5. Mineral chemistry of amphibole (wt.%) from phase 1 Oortsog rocks

Component	Peridotite	Ol melanogabbro		Troctolite	Ol mesogabbro					
	Mg Hbl	Aktinolite	Mg Hbl	Aktinolite	Aktinolite		Mg Hbl			Tremolite
SiO_2	52.92	53.33	52.18	54.57	52.74	55.62	46.15	48.28	51.36	54.97
TiO_2	0.40	0.12	0.25	0.18	0.19	0.77	0.51	1.08	0.57	0.02
Al_2O_3	2.53	3.33	6.04	2.88	2.61	2.58	11.75	7.47	5.84	1.93
Cr_2O_3	0.22	0.23	0.02	0.05	0.55	0.09	0.12	0.26	0.39	bdl
FeO	8.46	9.06	9.22	7.66	7.01	6.52	8.68	7.66	9.42	6.62
MnO	0.21	0.20	0.16	0.12	0.15	0.13	0.09	0.13	0.16	0.15
MgO	16.42	16.04	18.16	19.25	16.53	19.14	16.45	15.88	17.13	20.17
CaO	19.98	17.16	11.58	12.75	18.97	13.09	12.26	15.63	12.49	12.98
Na_2O	0.18	0.29	0.57	0.28	0.25	0.18	1.86	0.88	0.49	0.20
K_2O	bdl	0.07	0.19	0.04	0.04	bdl	0.36	bdl	0.16	0.02
Total	17.36	17.24	16.89	16.98	17.29	16.99	17.42	17.39	17.04	17.00
Mg/(Mg + Fe)	77.58	75.94	98.22	88.98	80.78	83.96	90.60	78.70	85.85	91.06

Table 6. Mineral chemistry of amphibole and biotite (wt.%) from phase 2 Oortsog rocks

Component	Peridotite	Ol melanogabbro		Ol mesogabbro				
	Mg Hbl	Mg Hbl		Tchermakite	Pargasite		Mg Hbl	Biotite
SiO_2	50.66	50.19	47.57	44.09	43.58	44.64	51.07	37.98
TiO_2	0.40	0.01	0.30	0.39	3.21	0.85	0.15	3.01
Al_2O_3	5.05	8.57	9.68	12.85	11.90	12.14	6.29	16.38
Cr_2O_3	0.09	0.02	0.05	0.16	0.13	0.29	0.05	0.17
FeO	10.15	5.77	8.45	9.25	8.39	7.56	5.96	8.27
MnO	0.19	0.13	0.17	0.13	0.09	0.10	0.12	0.02
MgO	17.36	20.48	17.59	15.96	15.47	16.53	19.59	19.59
CaO	11.27	11.57	12.16	10.74	11.21	11.54	12.43	0.02
Na_2O	0.60	0.86	1.46	2.14	2.30	2.10	1.08	1.23
K_2O	0.14	0.01	0.30	0.15	0.61	0.67	0.01	7.61
Total	15.19	15.23	15.46	15.63	15.66	15.72	15.30	94.28
Mg/(Mg + Fe)	78.05	94.95	85.16	78.63	76.68	79.84	89.05	–

yellow to dark brown and reddish. It forms a poikilitic texture together with Opx, Cpx and Pl (Fig. 2*c*, *d*), or sometimes is enclosed in Cpx. The biotite composition corresponds to the phlogopite endmember of the biotite series (19.6 wt.% MgO) in the Mg–Fe–Al ternary for iron-magnesian micas (Table 6).

Phase 2 rocks contain interstitial accessory apatite as ≤1 mm elongate grains.

Major-element chemistry

The Oortsog rocks have ultramafic and mafic major-element compositions with 36 to 48 wt.% SiO_2 increasing from ultramafic to anorthosite lithologies, and MgO contents of 5–35 wt.% in phase 1 and 17–25 wt.% in phase 2 (Fig. 5, Table 7). The contents of SiO_2, Na_2O and K_2O increase progressively (while MgO decrease) with the crystallization progress, i.e., alkalis accumulate as the system evolves. As silica and alkalis increase, Al_2O_3 and TiO_2 increase as well. Greater Al_2O_3 (Fig. 5*a*) and CaO contents at lower MgO are due to fractionation of olivine and plagioclase.

There are several prominent features of difference between the two phases in the Oortsog intrusion. MgO and total alkalis are in anticorrelation in phase 1 while the compositions of phase 2 plot a separate field in the diagram (Fig. 5*b*). Phase 2 rocks show greater enrichments in alkalis, especially K_2O (up to 0.8 against 0.2 wt.%), as well as in P_2O_5 and TiO_2 (0.06 and 0.50 wt.%, respectively) at 17–21 wt.% MgO (Fig. 5*c*, *d*). Incompatible elements differ markedly between the two phases, which indicates that they cannot be derived from the same parental melt. The enrichments of phase 2 rocks in Ti, P, and alkalis (especially, K) show up in the mineralogy including biotite, accessory apatite and Ti-magnetite, as well as Ti-bearing clinopyroxene (to 0.56 wt.% TiO_2).

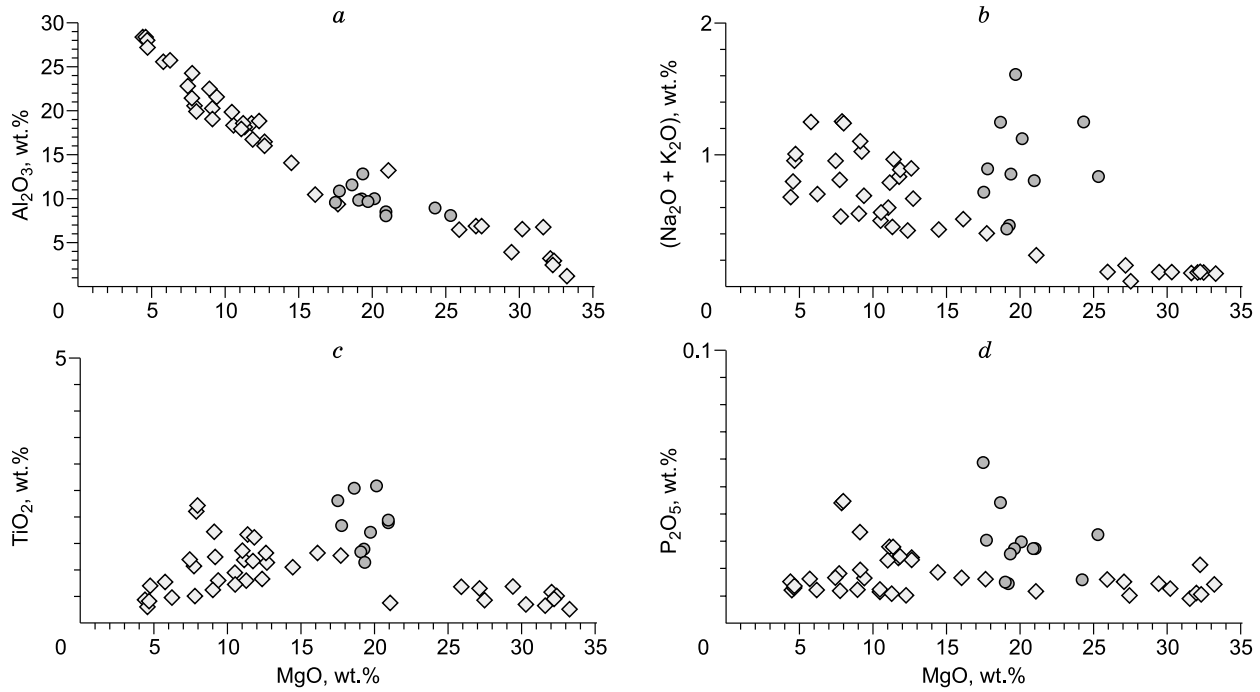

Fig. 5. MgO vs. Al_2O_3 (*a*), $(Na_2O + K_2O)$ (*b*), TiO_2 (*c*), P_2O_5 (*d*) in rocks of phases 1 and 2 of the Oortsog intrusion. See Fig. 4 for designations.

Trace-element chemistry

The Oortsog rocks are depleted in REE, with chondrite-normalized abundances within 10 units (Boynton, 1984), and reach the highest concentrations in biotite-bearing mesogabbro of phase 2 (Fig. 6*a*, Table 7). The REE patterns slope negatively (more prominent in phase 2) with slightly higher LREE, at $(La/Yb)_n$ = 2.24–3.05, and have flat HREE spectra, whereas the rocks with lower plagioclase percentages show positive REE slopes because of LREE depletion, with $(La/Yb)_n$ = 0.53–0.98. REE in the layered rocks of phase 1 increase generally from plagioperidotite to Ol-melanogabbro and show a typical positive Eu anomaly varying from 1.2 to 3.8 Eu/Eu* depending on the modal content of plagioclase.

The Oortsog rocks are also depleted in most of LILE, except for Sr, Cs and Ba, and HFSE, relative to N-MORB compositions (Sun and McDonough, 1989). Phase 1 rocks show positive anomalies in Cs, Sr, U and Eu and negative anomalies in HFSE (Th, Nb, Zr, Hf and Ti), while those of phase 2 have higher PM-normalized element contents (McDonough et al., 1992) than phase 1 (Fig. 6*b*), as well as highs in Cs (prominent) and Eu (weaker than in phase 1), and depletions in Ta and Nb.

The $^{147}Sm/^{144}Nd$ ratios (Table 8) are 0.136 (phase 1) and 0.151 (phase 2). The ε_{Nd} values are positive in rocks of phase 1 (+13.5, 270 Ma) and negative in those of phase 2 (−4.3, 270 Ma), which correspond to depleted and enriched mantle sources, respectively (White and Hofmann, 1982).

Modeling parental melt compositions for phase 1 and 2 rocks

The compositions of the Oortsog parental melts were modeled in terms of fractional crystallization using the *COMAGMAT 3.57* software (Ariskin et al., 1993), separately for rocks of the two phases. The assumptions for the conditions of magma emplacement were: a pressure of 2 kbar, an oxygen fugacity at the QFM (quartz–fayalite–magnetite) buffer, and a crystallinity degree of 90%. The obtained model composition trends agree with those of the real Oortsog rocks of phases 1 and 2 (Fig. 7). The parental melt with higher TiO_2 and alkalis corresponds to rocks of phase 2. The MgO contents in the melts are similar for the two phases, which rules out fractionation of one phase from another. The modeling predicts Mg basalt compositions of the parent melts in both cases (Table 9).

Age of the Oortsog intrusion

Oortsog was interpreted as an Early Paleozoic (PZ_1) intrusion according to the geological map of Khosbayar et al. (1987) and the data of Izokh et al. (1990). In this study, the age of the intrusion has been updated by the U–Pb and Ar–Ar methods applied to large-scale samples of olivine mesocratic gabbro of phase 1 (Sh-20-15) and olivine biotite-bearing mesogabbro of phase 2 (V-13057).

U–Pb zircon ages have been obtained for a few zircon grains extracted from phase 2 olivine mesogabbro (Fig. 8). Th/U ratios in zircons vary from 0.46 to 1.10 (Table 10), in the range common to mafic rocks (Xiang et al., 2011). The

concordia age (Fig. 9*a*) of the zircons is 272 ± 2 Ma, or Early Permian. All extracted grains are zoned and the Th/U ratios in the core (0.46–1.10) fall in the range of magmatic zircons (Hoskin and Schaltegger, 2003).

Ar–Ar dating was performed additionally for rocks of both phases by the stepwise heating $^{39}Ar/^{40}Ar$ method on amphibole from phase 1 olivine mesogabbro and biotite from phase 2 biotite-bearing olivine. The age spectra of the two minerals showed plateaus with 96% of released ^{39}Ar (Fig. 9*b*, *c*) at 278.7 ± 2.5 Ma (phase 1) and 257.3 ± 6.5 Ma (phase 2), which correspond to the Early/Middle Permian boundary.

The misfit between the U–Pb and Ar–Ar ages varies from 6.5 up to 23.0 Ma. The Ar–Ar date more likely records a later tectonic-magmatic event because the biotite K/Ar isotope system closes at 340 ± 20 °C (Hodges, 2004). Anyway, the updated age of the Oortsog intrusion is Permian rather than Early Paleozoic.

Ground-based magnetic survey of the Oortsog area

Ground-based magnetic survey was performed in the area of the Oortsog intrusion in 2015, and the data were used to map the anomalies of the magnetic induction vector, or magnetic flux density (**F**). The *magnetic field* was measured by an MMPOS-2 portable magnetometer with two POS-1 Overhauser sensors spaced at 1 m one over another, with the lower sensor 2 m above the ground surface (on a holder behind the operator's back). The magnetometer was run in an automatic mode, at a sampling rate of 3 s, which corresponds to 3–5 m spacing of points along profiles, depending on the walking speed of the operator. The points were positioned by GPS. The profiles were spaced at ~100 m. The magnetic filed variations were recorded by an MMPOS-1 station with a POS-1 Overhauser sensor, in the automatic mode, at every 5 s.

The recorded magnetic variations were normalized to a datum (the median of all measured **F** values) and averaged in a sliding window with a radius equal to the profile spacing. Then the data were interpolated over the entire study area on a uniform grid for mapping. The anomalies in the magnetic flux magnitude ($\mathbf{F}_a$) were accurate to 5%, as estimated from control measurements.

Magnetic susceptibility (Table 11) was measured with a KT-5 field kappameter to a resolution of 10^{-5} SI units, and

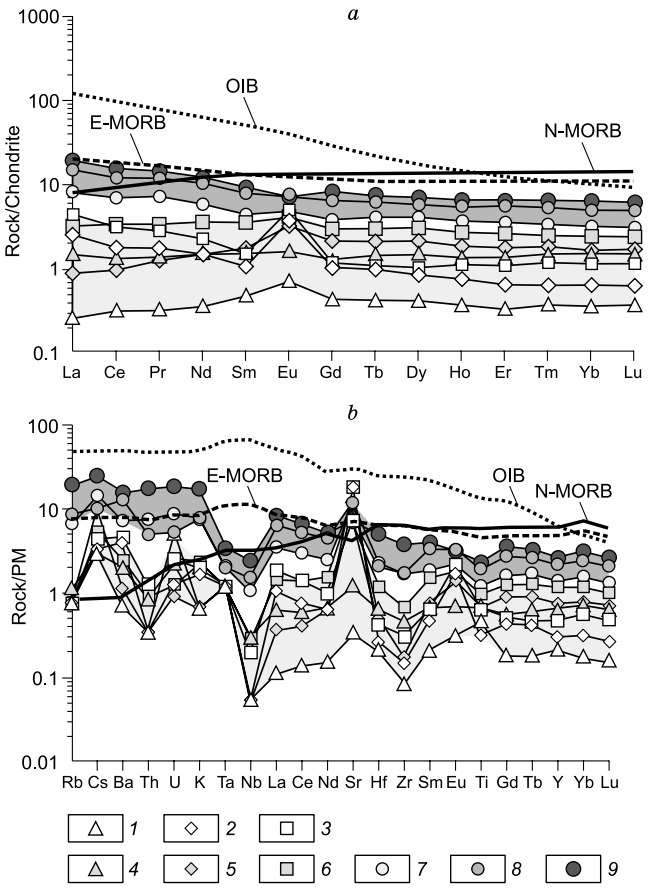

Fig. 6. *a*, REE spectra normalized to chondrite CI (Boynton, 1984); *b*, multielement spectra normalized to primitive mantle (McDonough et al., 1992). *1*, plagioperidotite; *2*, leucogabbronorite; *3*, mesogabbronorite; *4*, lherzolite; *5*, olivine mesogabbro; *6*, olivine melanogabbro; *7*, Bt-bearing leucogabbro; *8*, Bt-beairng olivine mesogabbro; *9*, Bt-bearing olivine mesogabbronorite. Different gray shades show domains of phases 1 and 2.

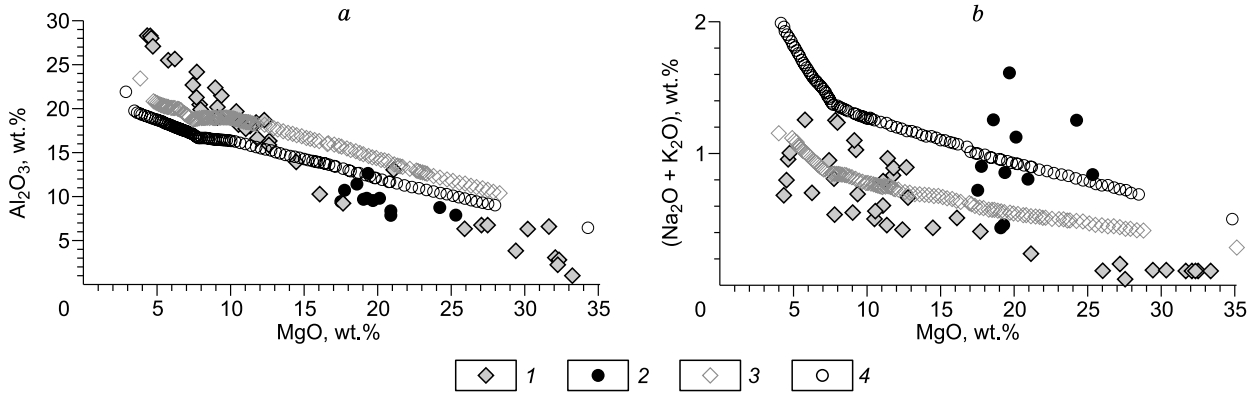

Fig. 7. Real (*1*, *2*) and model (*3*, *4*) compositions of phases 1 (*1*, *3*) and 2 (*2*, *4*) in the Oortsog intrusion, compared.

Table 7. Major- and trace-element compositions of Oortsog rocks: selected analyses

Component	Phase 1 rocks							Phase 2 rocks		
	Plagio-harzburgite	Lherzolite	Ol melanogabbro	Meso-gabbronorite	Leuco-gabbronorite	Ol mesogabbro	Ol mesogabbro	Bt-bearing olivine mesogabbronorite	Bt-bearing olivine mesogabbro	Bt-bearing leucogabbro
SiO_2, wt.%	34.76	39.83	46.19	45.57	44.00	45.28	44.84	47.05	46.84	48.25
TiO_2	0.10	0.14	0.21	0.14	0.07	0.15	0.15	0.51	0.27	0.43
Al_2O_3	2.37	3.84	14.10	27.18	28.38	18.45	19.80	11.53	15.90	20.48
Fe_2O_3	19.51	12.62	6.40	4.87	3.67	5.05	8.04	11.47	6.96	6.96
MnO	0.22	0.19	0.11	0.08	0.05	0.09	0.12	0.16	0.10	0.11
MgO	32.21	29.38	14.43	4.68	4.50	11.26	10.45	18.60	12.59	7.85
CaO	1.59	7.16	16.86	14.81	16.65	16.72	15.75	8.35	15.42	14.03
Na_2O	0.10	0.10	0.38	0.96	0.76	0.42	0.55	1.11	0.69	1.03
K_2O	0.02	0.02	0.07	0.06	0.05	0.04	0.02	0.51	0.22	0.23
P_2O_5	0.01	0.01	0.02	0.01	0.01	0.01	0.01	0.04	0.02	0.04
LOI	9.03	6.47	0.80	0.36	1.34	2.45	0.33	0.42	0.44	0.44
Total	100.52	100.22	99.93	98.80	99.62	100.17	100.21	100.25	99.67	100.17
Rb, ppm	0.50	0.75	0.50	0.50	0.50	0.76	0.50	12.82	4.26	5.60
Cs	0.10	0.10	0.18	0.14	0.11	0.15	0.32	0.82	0.46	0.34
Ba	5.19	14.41	17.27	32.42	27.94	13.49	8.08	112.39	51.50	92.04
Sr	7.37	26.28	157.41	392.48	396.25	208.12	247.56	151.80	182.55	254.75
Th	0.03	0.07	0.08	0.11	0.03	0.03	0.03	1.50	0.64	0.43
U	0.11	0.05	0.03	0.05	0.03	0.02	0.02	0.40	0.19	0.11
La	0.08	0.46	1.02	1.37	0.78	0.54	0.27	5.98	2.55	4.63
Ce	0.26	1.10	2.71	2.57	1.43	1.38	0.78	12.49	5.61	9.80
Pr	0.04	0.17	0.42	0.35	0.22	0.24	0.15	1.79	0.89	1.46
Nd	0.21	0.91	2.15	1.37	0.89	1.23	0.90	7.38	3.51	6.28
Sm	0.10	0.30	0.70	0.29	0.21	0.51	0.35	1.82	0.86	1.55
Eu	0.05	0.12	0.31	0.38	0.28	0.27	0.24	0.54	0.36	0.57
Gd	0.11	0.34	0.76	0.31	0.27	0.64	0.56	2.16	0.99	1.68
Tb	0.02	0.07	0.14	0.05	0.05	0.11	0.10	0.36	0.19	0.30
Dy	0.13	0.48	1.00	0.33	0.27	0.76	0.70	2.27	1.31	1.85
Ho	0.03	0.10	0.20	0.08	0.05	0.14	0.13	0.48	0.27	0.40
Er	0.07	0.29	0.56	0.23	0.13	0.40	0.38	1.36	0.75	1.16
Tm	0.01	0.05	0.08	0.04	0.02	0.06	0.06	0.21	0.11	0.17
Yb	0.08	0.31	0.51	0.24	0.13	0.39	0.34	1.35	0.67	1.05
Lu	0.01	0.05	0.08	0.04	0.02	0.06	0.05	0.20	0.10	0.16
Zr	0.95	5.24	7.63	3.48	1.65	3.40	1.97	43.64	19.42	19.97
Hf	0.07	0.20	0.38	0.13	0.08	0.16	0.16	1.60	0.72	0.67
Nb	0.04	0.21	0.21	0.14	0.04	0.09	0.04	1.76	0.79	1.11
Ta	0.05	0.05	0.05	0.05	0.05	0.05	0.05	0.14	0.09	0.09
Y	0.98	2.94	5.52	2.20	1.42	3.82	3.47	12.26	6.66	10.26
Eu/Eu*	0.65	6.00	21.00	4.29	5.00	20.00	18.77	3.43	4.00	10.25
$(La/Yb)_n$	4.30	18.26	42.98	27.34	17.78	24.58	18.00	52.00	39.30	73.68

Note. Whole-rock element contents were analyzed by XRF at the Analytical Center for Multielement and Isotope Studies, Novosibirsk (analyst N.G. Karmanova). Trace-element contents were analyzed by ICP–MS (analyst I.V. Nikolaeva).

average values were calculated over every three measurements. The map of magnetic (**F**) anomalies shows two distinct zones of 200 to 600 nT and –200 to 0 nT (Fig. 10), as well as numerous terrain-related heterogeneities and local lows presumably associated with minor amounts of remnant country rocks.

According to the geological setting (see above), the revealed magnetic field zones may represent the Oortsog rocks

Table 8. Sm–Nd ratios in Oortsog rocks of phases 1 and 2

Sample	Lithology	Age, Ma	Sm	Nd	$^{147}Sm/^{144}Nd$	$^{143}Nd/^{144}Nd$	Err	$\varepsilon_{Nd}(0)$	$\varepsilon_{Nd}(T)$
Phase 1									
Ch-30-14/2	Plagioperidotite	260.00	0.141	0.623	0.136	0.513	15	11.44	13.5
Phase 2									
V-13057	Bt-bearing Ol-mesogabbro	260.00	1.488	5.934	0.152	0.512	14	–5.83	–4.3

Note. Data were obtained by TIMS at the Geological Institute, Kola Science Center, Apatity (analyst A.S. Serov).

Table 9. Major-oxide compositions of parental melts for Oortsog rocks (wt.%)

Phase	SiO_2	TiO_2	Al_2O_3	FeO	MgO	CaO	Na_2O	K_2O	P_2O_5	∑
Phase 1	42.88	0.16	15.45	8.39	16.21	12.38	0.54	0.07	0.02	96.1
Phase 2	46.49	0.36	13.34	8.20	16.17	11.24	0.74	0.28	0.03	96.85

Table 10. U–Pb ages of zircons from phase 2 Oortsog rocks (V-13057)

Grain No.	$^{206}Pb_c$, %	U ppm	Th ppm	$^{232}Th/^{238}U$	$^{206}Pb^*$, ppm	$^{206}Pb/^{238}U$		$^{207}Pb/^{206}Pb$		$^{238}U/^{206}Pb^*$	± %	$^{207}Pb^*/^{206}Pb^*$	± %	$^{207}Pb^*/^{235}U$	± %	$^{206}Pb^*/^{238}U$	± %
1.1	–	466	285	0.63	17.4	275.2	± 2.7	446	±140	22.93	1	0.0558	6.4	0.336	6.5	0.04362	1.00
2.1	0.04	518	226	0.45	19.5	275.8	± 2.4	170	± 50	22.87	0.87	0.0495	2.1	0.2981	2.3	0.04372	0.87
3.1	–	1212	1290	1.10	45	273.1	± 2.0	235	± 34	23.11	0.76	0.05088	1.5	0.3036	1.7	0.04327	0.76
4.1	–	424	314	0.76	15.6	272	± 2.6	481	±120	23.21	0.98	0.0567	5.4	0.337	5.5	0.04309	0.98
5.1	–	787	582	0.76	29.1	271.7	± 2.2	255	± 42	23.23	0.81	0.05131	1.8	0.3046	2.0	0.04305	0.81
6.1	0.04	626	285	0.47	23	270.2	± 2.2	183	± 66	23.36	0.85	0.0497	2.8	0.2936	3.0	0.04281	0.85
7.1	0.13	410	314	0.79	15.1	270.2	± 2.8	336	± 58	23.36	1.1	0.0532	2.6	0.3138	2.8	0.0428	1.10
8.1	–	399	315	0.82	14.9	275.2	± 2.6	256	± 84	22.93	0.97	0.0513	3.7	0.309	3.8	0.04361	0.97
10.1	–	321	143	0.46	11.9	272.5	± 2.6	350	± 61	23.16	0.97	0.0535	2.7	0.3185	2.8	0.04317	0.97

Note. Ages were determined at the Center for Isotope Studies of Russian Research Geological Institute, St. Petersburg (analyst A.N. Larionova).

of phases 1 and 2. Correspondingly, the magnetic susceptibility is relatively high in rocks of phase 1 and low in those of phase 2: $(11–46)\times10^{-3}$ SI units and $(0.3–7)\times10^{-3}$ SI units, respectively (Table 11). The difference is due to high percentages of magnetite and pyroxene in phase 1 rocks (Kobranova, 1986), especially in peridotite occurring near the intrusion top. The presence of these rocks is confirmed by the map of magnetic anomalies and petrography. The magnetic susceptibility of sulfide-bearing rocks increases proportionally to sulfide saturation, because pyrrhotite is a strongly magnetic mineral, as well as to the contents of less magnetic biotite (Dortman, 1984). The geophysical data added to the simplified geological map of the intrusion (Fig. 10) have provided updates to its structure (Fig. 1).

DISCUSSION

The Oortsog rocks contain ubiquitous calcic plagioclase with $An_{90–96}$ (Table 2), which allows classifying the troctolite and gabbro of phases 1 and 2 as *allivalite* and *eucrite*, respectively (Bogatikov et al., 2009). The presence of high-An plagioclase may result from high contents of H_2O that buffers Na in the melt and thus maintains Ca enrichment of rocks (Pletchov and Gerya, 1998). Such plagioclase is of rare natural occurrence and is restricted to a few mafic–ultramafic intrusions (Bayan-Tsagan, Hayarhan, etc.) in Mongolia (Galakhova, 1963).

Mao et al. (2018) likewise suggested the presence of two rock groups in the Oortsog intrusion, which emplaced in two events, proceeding from difference in Ni contents and inconsistent changes in the Fo component discordant with the fractional crystallization trend. Our data support this hypothesis and indicate that the two phases formed in different conditions (see below).

Each rhythm of the layered intrusion includes different lithologies arranged inversely from base to top (relative to the present position of the intrusion): leucogabbro, mesogarbbro, troctolite, melanotroctolite, and peridotite. This succession contradicts the normal pattern with melanocratic rocks grading toward more leucocratic lithologies from the base to top of rhythms according to the fractional crystalliza-

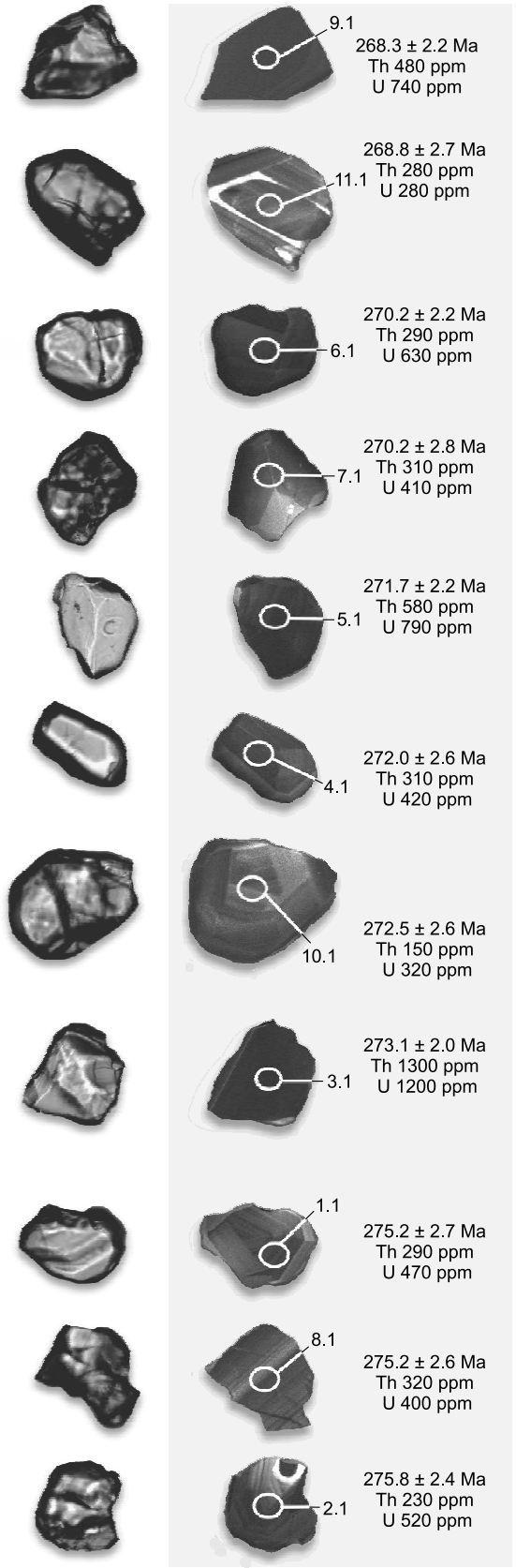

Fig. 8. Morphology, structure, and age of zircon grains from phase 2 gabbro (sample V-13057) in the Oortsog intrusion. Left: reflected light image; right: CL image.

tion sequence (Wager and Brown, 1967; Sharkov, 1980). The petrographic data agree with major-element chemistry: MgO increases progressively up the section (in the present position) and within each rhythm, but decreases abruptly at each layer boundary (Fig. 3). However, other known rhythmically layered intrusions show an opposite MgO trend: decreasing generally upsection and increasing on transitions to each following rhythm (Polyakov et al., 1984; McBirney, 1996). Therefore, the Oortsog intrusion may be tectonically upset, which does not contradict the geological map (Khosbayar et al., 1987) which shows folded Early Proterozoic and Early Mesozoic (Carboniferous and Triassic) country rocks, with overturned folding in the area of the Hangayn Mountains. Thus, all sedimentary and igneous rocks of the region, including the Oortsog intrusion, were involved into folding which led to the structural changes. The overturned position of the intrusion revealed from petropgraphic and major-element signatures is consistent with large-scale structures in the area. The inverse zoning (upward decrease in melanocratic components) might be due to earlier crystallization of plagioclase than olivine, judging by the absence of early euhedral plagioclase crystals in melanocratic rocks. Therefore, it is reasonable to infer a tectonically upset position of the Oortsog intrusion, which was deformed together with the country rocks.

The revealed magnetic anomalies are highly contrasting and allow contouring the exposures of two rock types (Fig. 11). In the northeastern part of the area, the anomalies are not always attributable to geological structures because of terrain effects. However, geophysical data agree with petrological evidence: rocks with relatively high and low magnetic susceptibility fall within the zones of positive and negative magnetic anomalies and correspond to rocks of phases 1 and 2, respectively. The map of magnetic anomalies shows that phase 1 peridotite lying in the upper part of the layered sequence also has the highest magnetic susceptibility (Table 11), which is consistent with the presence of more melanocratic rocks in the upper section and confirms the idea that the intrusion has been overturned.

The rocks of phases 1 and 2 differ markedly in major- and trace-element chemistry and were apparently emplaced in two different events. The dissimilarity of incompatible element patterns between the rocks of the two phases, at similar concentrations of MgO (Fig. 4), rules out their crystallization from the same parental melt by a continuous fractionation process (Kovalenko, 1987). Trace and rare-earth elements in phase 2 rocks are much higher, i.e., the parental melt was more strongly fractionated than that for phase 1. The difference in ε_{Nd} values, which are positive for phase 1 and negative for phase 2, is another argument against successive fractional crystallization of the two phases from the same melt: rocks with such ε_{Nd} difference are expected to originate from different mantle sources, possibly, at different depths (Vrevsky et al., 1996; Polat et al., 1999). Phase 2 was likely derived from enriched mantle, judging by higher TiO_2 (to 0.6 wt.%) and alkalis (to 1.8 wt.%), as well as by

Table 11. Magnetic susceptibility of Oortsog rocks

Sample	Lithology	Magnetic susceptibility 10^{-3} SI units	Sample	Lithology	Magnetic susceptibility, 10^{-3} SI units
Phase 1			Phase 2		
V13048	Melanogabbro with sulfides	11.8	V-13043	Melanogabbro with sulfides	5.34
V13050	peridotite	46.05	V-13044	Ol gabbro	2.86
CH-2-14	Gabbronorite with sulfides	3.1	V-13045	Ol melanogabbro with sulfides	3.25
CH-4-14	Melanocratic troctolite	17.5	V-13046	Gabbro with sulfides	6.01
CH-5-14	Plagioperidotite	29.7	V-13052	Gabbro with sulfides	6.62
CH-8-14	Ol melanogabbro	0.56	V-13056	Gabbro with sulfides	2.52
CH-10-14	Ol mesogabbro	0.18	V-13057	Bt-bearing Ol melanogabbro	1.8
CH-25-14	Plagioperidotite	28.1	V-13058	Mesogabbro with sulfides	6.6
CH-28-14	Amphibole gabbro	0.18	V-13059	Melanogabbro with sulfides	4.68
CH-30-14	Dunite	35.3	V-13060	Mesogabbro with sulfides	7.09
CH-31-14	Ol mesogabbro with sulfides	3.05	V-13062	Gabbro with sulfides	2.7
CH-32-14	Amphibole gabbro	0.22	MO-2-16	Leucogabbro	0.86
CH-34-14	Leucogabbro	0.65	MO-3-16	Bt-bearing leucogabbro	2.38
CH-36-14	Ol mesogabbro	0.12	MO-4-16	Leucogabbro	1.04
MO-11-16	Leucogabbro	1.12	MO-5-16	Bt-bearing leucogabbro	4.94
MO-12-16	Leucogabbro	1.1	MO-6-16	Leucogabbro	0.33
MO-15-16	Mesogabbro	0.63	MO-7-16	Bt-bearing leucogabbro	4.28
MO-16-16	Mesogabbro	0.56	MO-8-16	Leucogabbro	1.43
MO-18-16	Mesogabbro	0.58	MO-23-16	Bt-bearing leucogabbro	3.25

Note. Rocks of CH-2-14 to CH-32-14 remain beyond the map of magnetic anomalies (Fig. 11).

negative ε_{Nd} (–4.3), whereas phase 1 with positive ε_{Nd} =13.5 rather had a depleted source (White and Hofmann, 1982). The existence of two mantle sources is also consistent with difference in Sm–Nd signatures. The calculated melt compositions differ especially in the contents of alkalis (COMAGMAT data, Table 9).

The rocks of phase 1, with positive ε_{Nd} values, HFSE depletion and LILE enrichment (Fig. 6), bear signatures of suprasubduction basaltic magmas (Izokh et al., 2005). Unlike these, the phase 2 rocks are markedly enriched in LREE, Ti and Nb, and their source may be associated with a mantle plume (Hofmann, 1997). Plume-related Nb enrichment is a well-known fact (Sun and McDonough, 1989), while suprasubduction tracers in rocks not always provide unambiguous evidence for the mantle wedge origin of magmatism. For instance, some rocks from Western Transbaikalia bear suprasubduction trace-element signatures (Tsygankov et al., 2010), but Late Paleozoic–Early Mesozoic magmatism in the area developed upon continental crust beyond any subduction zone. Therefore, constraining the tectonic setting in this case is challenging and requires further investigation.

There are other intrusions with plume and suprasubduction signatures elsewhere in CAOB. Namely, the Surovo intrusion (East Kazakhstan) in the Kalba–Narym zone of the Altai collisional system likewise comprises two rock groups: low-alkali olivine–pyroxene–plagioclase gabbro corresponding to low-K tholeiite series and subalkaline amphibole–biotite gabbronorite corresponding to moderately potassic calc-alkaline series (Khromykh et al., 2016), which presumably originated from different magmas. Mafic magmatism in Eastern Kazakhstan spanned a period between 320 and 270 Ma (Khromykh et al., 2016), which is consistent with the age of magmatism in Mongolia (Early Permian–Late Carboniferous). That was also the time of magmatic activity associated with plume–lithosphere interaction (Khromykh et al., 2016) that produced the Tarim–Mongolia large igneous province (Kuzmin and Yarmoluk, 2014; Xu et al., 2014).

Spatially proximal and coeval gabbro of different compositions were also reported from the Krestovsky zone of the Olkhon area (Western Baikal region): phase 2 gabbro of the Birkhin complex differ from rocks of phase 1 in higher contents of incompatible elements, a negative Ta–Nb anomaly and a positive Sr anomaly, which was attributed to a suprasubduction component in the magma source (Lavrenchuk et al., 2017). The formation of chemically different gabbro within the same crust zones, one shortly after another, may be evidence of a tectonic setting change: subduction–accretion–collision–hotspot activity. Magmas of different phases form under the hot field effect: first without and then with enriched material involved.

Thus, the Oortsog rocks are compositionally similar to mafic complexes from Eastern Kazakhstan (Khromykh et al., 2016) and the Olkhon area (Lavrenchuk et al., 2017).

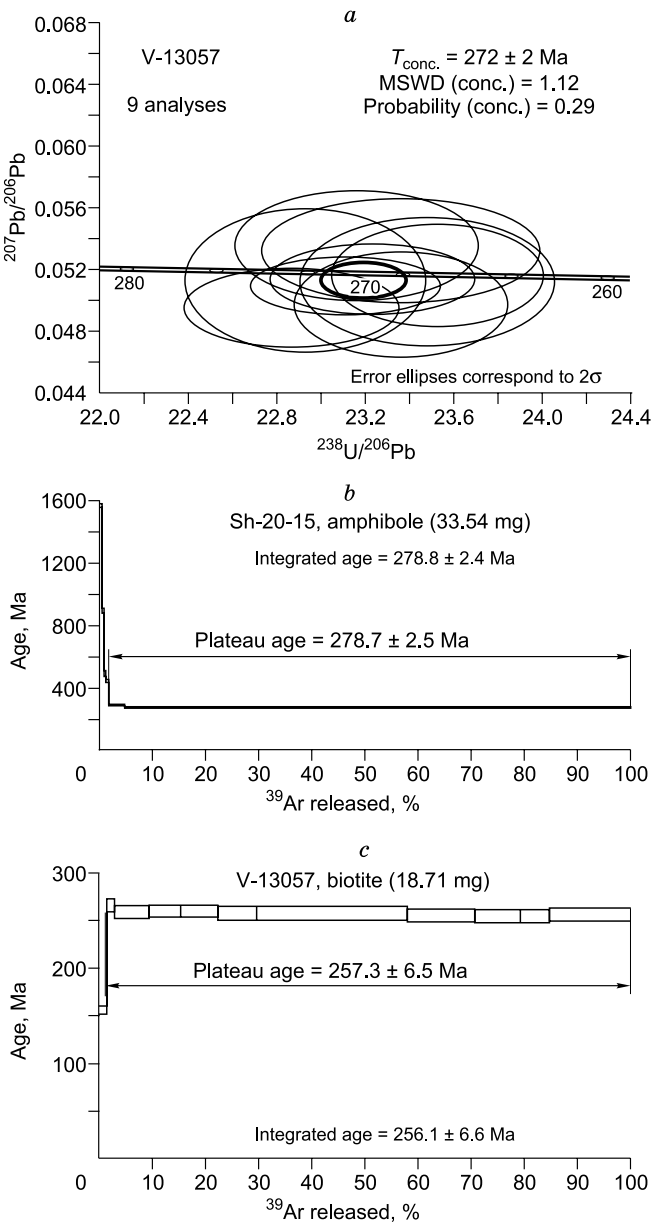

Fig. 9. Age of the Oortsog intrusion: *a*: concordia diagram for zircons from phase 2 rocks; *b*, *c*: stepwise heating Ar–Ar age spectra of phase 1 amphibole and phase 2 biotite.

Rocks of phase 2 have higher contents of LREE, Ti, K, and P than those of phase 1. The intrusions from the three areas emplaced in two events, with a short time gap, and had two magma sources.

Although being updated by the new determinations, the age of the Oortsog intrusion remains uncertain. Phase 1 has been dated by the Ar–Ar method only (on Mg hornblende), at 278 ± 2.5 Ma, while phase 2 has received an Ar–Ar biotite age of 257 ± 6.5 Ma and a U–Pb zircon age of 272 ± 2 Ma. Anyway, dating by different methods does not confirm the Early Paleozoic (PZ_1) age shown in the geological map (Khosbayar et al., 1987). The 7 to 15 Ma misfit between the Ar–Ar and U–Pb ages for phase 2 may have two explanations: (i) the two isotope systems closed at different times which may occur either when magma cools down slowly or when it reheats to lower temperatures (Dodson, 1973); (ii) the analyzed zircons may be xenogenic, captured from the wallrock. In the latter case, the zircon age would correspond to the lower age bound of phase 2, which is thus no older than 272 ± 2 Ma.

Thus, both explanations support a Permian (rather than Early Paleozoic) emplacement age for the Oortsog intrusion. Note that there are several other Permian intrusions in the region: the Nomgon (256 ± 2.1 Ma) (Izokh et al., 1998) and Nariyntol-Buriyn-Gol (249–252 Ma) (Izokh et al., 1990) intrusions in Mongolia and ~274 Ma mafic–ultramafic intrusions in Northwestern China (Mao et al., 2014), some with PGE mineralization (Izokh et al., 1992; Mao et al., 2015, 2017). There are reasons to believe that the Oortsog intrusion, together with other Permian intrusions in Mongolia within CAOB, are products of Permian magmatism related to a single large igneous province. The Oortsog rocks may also have a PGE potential as well (Mao et al., 2018).

The obtained age constraints for the two phases have some implications for the tectonic setting of the Oortsog intrusion: whether it belongs to the Tarim large igneous province or is associated with active continental margin mafic–ultramafic magmatism. The active margin of the Mongolia–Siberia continent existed in the latest Middle Paleozoic in the folded periphery of the southern Siberian craton (Gordienko, 1987), and Late Paleozoic intrusion events (257–278 Ma) were possible in that setting. On the other hand, magmatism in the CAOB territory maintained by the Mongolian hotspot (Yarmoluk and Kuzmin, 2012) acted within the continental margin and led to the formation of the Tarim–South Mongolia igneous province which had completed by 280–275 Ma. Then the plume activity moved to the Hangayn area (270–240 Ma) and on into Eastern Mongolia and Transbaikalia in the Early Mesozoic. This migration of within-plate magmatism is quite consistent with clockwise rotation of Siberia whereby its active margin passed over the Mongolian mantle hotspot (Kuzmin et al., 2010; Yarmoluk et al., 2012). According to this model, the Oortsog intrusion belongs to the Tarim LIP. More insights into the tectonic setting of magmatism in the Hangayn region can be gained through further comprehensive studies with reference to data from other gabbro intrusions.

CONCLUSIONS

New data from the Oortsog intrusion lead to the following inferences.

1. Petrography (upsection changes from leucocratic to melanocratic lithologies in each rhythm), major-element chemistry (MgO increase in each rhythm and generally over the section), as well as the data of magnetic surveys indicate that the intrusion position changed upside down during a

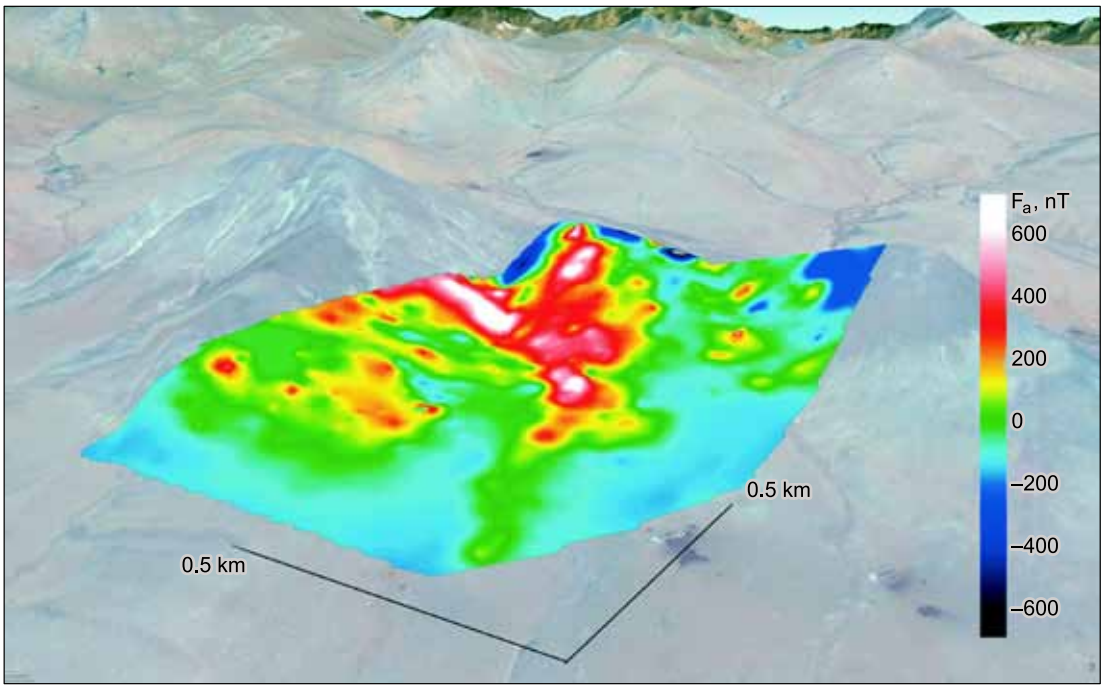

Fig. 10. Magnetic anomalies and superposed terrain.

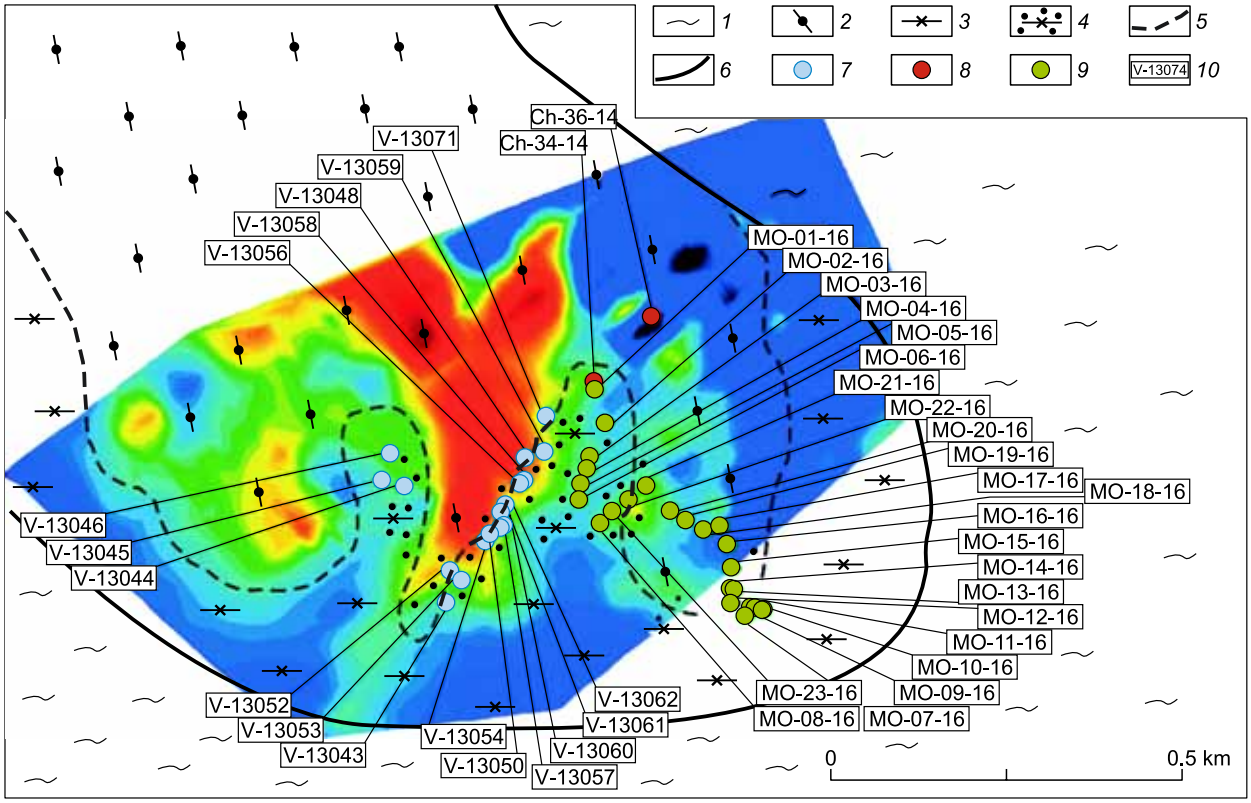

Fig. 11. Magnetic anomalies and superposed intrusion contours. *1*, schist and gneiss; *2*, phase 1 gabbro; *3*, phase 2 gabbro; *4*, gabbro with disseminated sulfide mineralization; *5*, boundary between phases 1 and 2; *6*, intrusion margin; *7*, samples of 2013; *8*, samples of 2014; *9*, samples of 2016; *10*, sample number.

tectonic event together with the host sediments which underwent overturned folding.

2. The Oortsog intrusion consists of two phases that differ in major- and trace-element signatures in rocks. The two phases apparently were derived from different mantle sources, judging by dissimilarity in the contents of incompatible elements and similarity in MgO: depleted mantle for rocks of phase 1 with ε_{Nd} = 13.5 calculated for the 270 Ma model age and enriched mantle for phase 2 with ε_{Nd} (270 Ma) = −4.3.

3. The reconstructed parental melts for both phases correspond to picritic basalt magmas with MgO contents of 16.21 wt.% (phase 1) and 16.17 wt.% (phase 2). The parental melt of phase 2 had greater enrichment in LREE (Rb, Ba, Cs, U, Th) and in Na, K and Ti, and produced high-alkali high-Ti gabbro.

4. Both phases have Permian isotope ages: 278 ± 2.5 Ma for phase 1 (Ar–Ar) and 272 ± 2 Ma (U–Pb) and 257 ± 6.5 Ma (Ar–Ar, system closure) for phase 2. There are all reasons to assign the Oortsog intrusion to the Permian large igneous province in the Central Asian Orogenic Belt.

We wish to thank the team of the Laboratory for Petrology and Metallogeny of Igneous Rocks at the V.S. Sobolev Institute of Geology and Mineralogy (IGM, Novosibirsk) for valuable advice and assistance in working with data. High-quality analytical work was provided by N.G. Karmanova, O.S. Khmelnikova, I.V. Nikolaeva, and D.S. Yudin from the Analytical Center of IGM (Novosibirsk), A.N. Larionova (Center for Isotope Research at the Russian Research Geological Institute (VSEGEI, St. Petersburg), and A.S. Serov from the Geological Institute of the Kola Science Center (Apatity).

The study was carried out as part of the government assignment to IGM (Project 0330-216-003) and was additionally supported by the Russian Foundation for Basic Research (Projects 16-35-00100, 16-05-00980, and 17-05-00825).

REFERENCES

Ariskin, A.A., Frenkel, M.Yr., Barmina, G.S., Nielsen, R.L., 1993. COMAGMAT: a Fortran program to model magma differentiation processes. Comput. Geosci. 19 (8), 1155–1170.

Badarch, G., Cunningham, W.D., Windley, F.B., 2002. A new terrane subdivision for Mongolia: Implications for the Phanerozoic crustal growth of Central Asia. J. Asian Earth Sci. 21 (1), 87–110.

Bogatikov, O.A., Morozov, A.F., Petrov, O.V. (Eds.), 2009. Petrographic Code [in Russian]. VSEGEI, St. Petersburg.

Boynton, W.V., 1984. Geochemistry of the rare earth elements: meteorite studies, in: Rare Earth Element Geochemistry. Elsevier, New York, pp. 63–114.

Dergunov, A.B., Luvsandazan, B., Pavlenko, V.S., 1980. Geology of Western Mongolia [in Russian]. Nauka, Moscow.

Dodson, M.N., 1973. Closure temperature in cooling geochronological and petrological systems. Contrib. Mineral. Petrol. 40 (3), 259–274.

Dortman, N.B., 1984. Physical Properties of Rocks and Mineral Deposits (Rock Physics) [in Russian]. Nedra, Moscow.

Ernst, R.E., 2014. Large Igneous Provinces. Cambridge University Press, Cambridge.

Ernst, R.E., Hamilton, M.A., Söderlund, U., Hanes, J.A., Gladkochub, D.P., Okrugin, A.V., Kolotilina, T., Mekhonoshin, A.S., Bleeker, W., Lecheminant, A.N., Buchan, K.L., Chamberlain, K.R., Didenko, A.N., 2016. Long-lived connection between southern Siberia and northern Laurentia in the Proterozoic. Nat. Geosci. 9 (6), 464–469.

Galakhova, O.M., 1963. Ball lavas in northwestern Mongolia, in: The Russian and Siberian Cratons and Their Folded Surroundings [in Russian]. Izd. AN SSSR, Moscow, pp. 176–195.

Gordienko, I.V., 1987. Paleozoic Magmatism and Geodynamics of the Central Asian Orogenic Belt [in Russian]. Nauka, Moscow.

Hodges, K.V., 2004. Geochronology and thermochronology in orogenic system, in: Treatise on Geochemistry. Elsevier, Vol. 3-9, 263–292.

Hofmann, A.W., 1997. Mantle geochemistry: the message from oceanic volcanism. Nature 385, 219–229.

Hoskin, P.W.O., Schaltegger, J.M., 2003. The composition of zircon and igneous and metamorphic petrogenesis. Rev. Mineral. Geochem. 53 (1), 27–62.

Izokh, A.E., Polyakov, G.V., Krivenko, A.P., Bognibov, V.I., Bayarbileg, L., 1990. Gabbro in Western Mongolia [in Russian]. Novosibirsk, Nauka.

Izokh, A.E., Mayorova, O.N., Lavrentiev, Yu.G., 1992. Minerals of the platinum metals in the Nomgon troctolite–anorthozite–gabbro intrusive massif (Mongolia). Geologiya i Geofizika (Russian Geology and Geophysics) 33 (1), 104–110 (87–92).

Izokh, A.E., Polyakov, G.V., Gibsher, A.S., Balykin. P.A., Zhuravlev, D.Z., Parkhomenko, V.A., 1998. High-alumina stratified gabbroids in the Central-Asian fold belt: geochemistry, Sm–Nd izotopic age, and geodynamic conditions of formation. Geologiya i Geofizika (Russian Geology and Geophysics) 39 (11), 1565–1577 (1565–1577).

Izokh, A.E., Shelepaev, R.A., Lavrenchuk, A.V., Borodina, E.V., Egorova, V.V., Vasyukova, E.A., Gladkochub, D.P., 2005. Diversity of Cambrian–Ordovician mafic–ultramafic assemblages of the Central Asian Orogenic Belt: a record of plume–lithospheric mantle interaction, in: Proc. Conf. Geodynamic Evolution of Lithosphere in the Central Asian Orogenic Belt (from Ocean to Continent) [in Russian]. IZK, Irkutsk, Book 1, pp. 106–109.

Khosbayar, P., Byamba, B., Binderiya, T., Gansukh, Z., 1987. 1:200,000 Geological Map. Ugiynuur Region [in Russian], L-48-I, II.

Khromykh, S.V., Tsygankov, A.A., Kotler, P.D., Navozov, O.V., Kruk, N.N., Vladimirov, A.G., Travin, A.V., Yudin, D.S., Burmakina, G.N., Khubanov, V.B., Buyantuev, M.D., Antsiferova, T.N., Karavaeva, G.S., 2016. Late Paleozoic granitoid magmatism of Eastern Kazakhstan and Western Transbaikalia: plume model test. Russian Geology and Geophysics (Geologiya i Geofizika) 57 (5), 773–789 (983–1004).

Kislov, E.V., 1998. Yoko-Dovyren Layerd Intrusion [in Russian]. BNC SO RAN, Ulan-Ude.

Kobranova, V.N., 1986. Rock Physics [in Russian]. Nedra, Moscow.

Kovalenko, V.I. (Ed.), 1987. Igneous Rocks, Vol. 6: Evolution of Magmatism in the Earth's History [in Russian]. Nauka, Moscow.

Kuzmin, M.I., Yarmolyuk, V.V., 2014. Mantle plumes in Northeastern Asia and their role in the formation of endogeneous deposits. Russian Geology and Geophysics (Geologiya i Geofizika) 55 (2), 120–143 (153–184).

Kuzmin, V.I., Yarmolyuk, V.V., Kravchinsky, V.A., 2010. Phanerozoic hot spot traces and paleogeographic reconstruction of the Siberian continent based on interaction with the African large low shear velocity province. Earth Sci. Rev. 102, 29–59.

Lavrenchuk, A.V., Sklyarov, E.V., Izokh, A.E., Kotov, A.B., Salnikova, E.B., Fedorovskii, V.S., Mazukabzov, A.M., 2017. Compositions of gabbro intrusions in the Krestovsky zone (western Baikal region): a record of plume–suprasubduction mantle interaction. Russian Geology and Geophysics (Geologiya i Geofizika) 58 (10), 1139–1153 (1439–1458).

Leake, B.E., Woolley, A.R., Arps, C.E.S., Birch, W.D., Gilbert, M.C., Grice, J.D., Hawthorne, F.C., Kato, A., Kisch, H.J., Krivovichev, V.G., Linthout, K., Laird, J., Mandarino, J.A., Maresch, W.V., Nickel, E.H., Rock, N.M.S., Schumacher, J.C., Smith, D.C., Stephenson, N.C.N., Ungaretti, L., Whittaker, E.J.W., Youzhi, G., 1997. Nomenclature of amphiboles: Report of the subcommittee on amphiboles of the International Mineralogical Association, Commission on New Minerals and Mineral Names. Am. Miner. 82, 1019–1037.

Luo, W., Zhanga, Z., Santosha, M., Houa, T., Huanga, H., Zhua, J., Wanga, X., Fua, X., 2014. Petrology and geochemistry of Permian mafic–ultramafic intrusions in the Emeishan large igneous province, SW China: Insight into the ore potential. Ore Geol. Rev. 56, 258–275.

Mao, Y.J., Qin, K.Z., Li, C., Xue, S.C., Ripley, E.M., 2014. Petrogenesis and ore genesis of the Permian Huangshanxi sulfide ore-bearing mafic–ultramafic intrusion in the Central Asian Orogenic Belt, western China. Lithos 200, 111–125.

Mao, Y.J., Qin, K.Z., Li, C., Tang, D.M., 2015. A modified genetic model for the Huangshandong magmatic sulfide deposit in the Central Asian Orogenic Belt, Xinjiang, western China. Miner. Deposita 50, 65–82.

Mao, Y.J., Qin, K.Z., Barnes, S.J., Tang, D.M., Xue, S.C., Vaillant, M. Le., 2017. Genesis of the Huangshannan high-Ni tenor magmatic sulfide deposit in the Eastern Tianshan, northwest China: Constraints from PGE geochemistry and Os–S isotopes. Ore Geol. Rev. 90, 591–606.

Mao, Y.J., Dash, B., Qin, K.Z., Bujinlkham, B., Tang, D.M., 2018. Comparisons among the Oortsog, Dulaan, and Nomgon mafic–ultramafic intrusions in central Mongolia and Ni–Cu deposits in NW China: implications for economic Ni–Cu–PGE ore exploration in central Mongolia. Russian Geology and Geophysics (Geologiya i Geofizika) 59 (1), 1–18 (3–22).

McBirney, A.R., 1996. The Skaergaard Intrusion. Developments in Petrology 15, 147–180.

McDonough, W.F., Sun, S.S., Ringwood, A.E., Jagoutz, E., Hofmann, A.W., 1992. Potassium, rubidium and cesium in the Earth and Moon and the evolution of the mantle of the Earth. Geochim. Cosmochim. Acta 56 (3), 1001–1012.

Morimoto, N., 1989. Nomenclature of Pyroxenes. Can. Mineral. 27, 143–156.

Nikolaeva, I.V., Palesskiy, S.V., Kozmenko, O.A., Anoshin, G.N., 2008. Analysis of geologic reference materials for REE and HFSE by inductively coupled plasma-mass spectrometry (ICP–MS). Geochem. Int. 10, 1016–1022.

Pletchov, P.Y., Gerya, T.V., 1998. Effect of H_2O on plagioclase-melt equilibrium. Experiment in GeoSciences 7 (2), 7–11.

Podlipsky, M.Yu., Mekhonoshin, A.S., Tolstykh, N.D., Vishnevskiy, A.V., Polyakov, G.V., 2015. Mineralogy and geochemistry of the Tartai massif, East Siberian metallogenic province. Geol. Ore Deposits 57 (3), 172–196.

Polat, A., Kerrich, R., Wyman, D., 1999. Geochemical diversity in oceanic komatiites and basalts from the late Archaean Wawa greenstone belts, Superior Province. Precambrian Res. 94 (3), 139–173.

Polyakov, G.V., Izokh, A.E, Bognibov, V.I., Krivenko, A.P., Bayarbileg, L., 1984. Early Paleozoic formation of stratified peridotite–pyroxenite–gabbronorite massifs of northwestern Mongolia. Geologiya i Geofizika (Soviet Geology and Geophysics) 25 (1), 50–62 (41–51).

Polyakov, G.V., Tolstykh, N.D., Mekhonoshin, A.S., Izokh, A.E., Podlipskii, M.Yu., Orsoev, D.A., Kolotilina, T.B., 2013. Ultramafic–mafic igneous complexes of the Precambrian East Siberian metallogenic province (southern framing of the Siberian craton): age, composition, origin, and ore potential. Russian Geology and Geophysics (Geologiya i Geofizika) 54 (11), 1319–1331 (1689–1704).

Shapovalova, M., Shelepaev, R., Tolstykh, N., Kalugin, V., Safonova, I., 2015. Petrology of the Ortsoog-Uul gabbro–peridotite PGE-bearing complex, Western Mongolia, in: Conf. 13th SGA Biennial Meeting 3, pp. 983–985.

Shapovalova, M.O., Shelepaev, R.A., Tolstykh, N.D., Kalugin, V.M., 2016. Composition of the Ortsoog-Uul peridotite–gabbro intrusion and related Cu–Ni–EPG mineralization (Western Mongolia), in: Topical Problems of Geology, Geophysics, and Geoenvironment of Northwestern Russia. Proc. XXVII Young-Carrier Conf. in Commemoration of K.O. Kratts, Corresponding Member of the USSR Academy of Sciences and F.P. Mitrofanov, Full Member of the USSR Academy of Sciences [in Russian], pp. 42–45.

Shapovalova, M.O., Tolstykh, N.D., Shelepaev, R.A., 2017. Petrology of the Ortsoog Uul peridotite–gabbro intrusion, Western Mongolia, in: Petrology of Igneous and Metamorphic Complexes [in Russian], Proc. IX All-Russian Petrographic Conf. with International Participants, pp. 455–460.

Sharkov, E.V., 1980. Petrology of Layered Intrusions [in Russian]. Nauka, Leningrad.

Sun, S., McDonough, W.F., 1989. Chemical and isotopic systematics of oceanic basalts: implications for mantle composition and processes, in: Magmatism in the Ocean Basins. Geological Society, London, Special Publications 42, pp. 313–345.

Svetlitskaya, T.V., Tolstykh, N.D., Izokh, A.E., Thi, P.N., 2015. PGE geochemical constraints on the origin of the Ni–Cu–PGE sulfide mineralization in the Suoi Cun intrusion, Cao Bang province, Northeastern Vietnam. Mineral. Petrol. 109 (5), 161–180.

Tomurtogoo, O. (Ed.), 2002. Tectonics of Mongolia. Atlas of 1:1,000,000 tectonic maps of Mongolia. Geological Information Center of the Mineral Resources Authority of Mongolia, Institute of Geology and Mineral Resources of the Mongolian Academy of Science.

Tsygankov, A.A., Khubanov, V.B., Filimonov, A.V., 2010. Bimodal volcanic and subvolcanic associations of Western Transbaikalia (PZ3–MZ): magma sources, evolution, and geodynamics. Litosfera 3, 78–86.

Vrevsky, A., Krimsky, R., Svetov, S., 1996. Isotopic (Nd, O) and geochemical (REE) heterogeneity of the Archaean mantle, Baltic Shield. in: Brewer, T.S. (Ed.), Precambrian Crust Evolution in the North Atlantic Region. Geological Society, London, Special Publication 112, pp. 43–54.

Wager, L.R., Brown, G.M., 1967. Layered Igneous Rocks. W.H. Freeman and Co., San Francisco.

White, W.M., Hofmann, A.W., 1982. Sr and Nd isotope geochemistry of oceanic basalts and mantle geochemistry. Nature 296, 821–825.

Xiang, W., Griffin, W.L., Jie, C., Pinyun, H., Xiang, L., 2011. U and Th contents and Th/U ratios of zircon in felsic and mafic magmatic rocks: improved zircon-melt distribution coefficients. Acta Geol. Sin. 85 (1), 164–174.

Xu, Y.G., Wei, X., Luo, Z.Y., Liu, H.Q., Cao, J., 2014. The Early Permian Tarim Large Igneous Province: Main characteristics and a plume incubation model. Lithos 204, 20–35.

Yanshin, A.L. (Ed.), 1974. Tectonic of Mongolia [in Russian]. Nauka, Moscow.

Yanshin, A.L., Zaitsev, N.S., Kovalenko, V.I., Luvsandanzan, B., Luchitskiy, I.V., Yarmolyuk, V.V., 1989. 1:1,500,000 Geological Map of Mongolia [in Russian]. Moscow.

Yarmolyuk, V.V., Kuzmin, M.I., 2012. Late Paleozoic and Early Mesozoic rare-metal magmatism of Central Asia: Stages, provinces, and formation settings. Geol. Ore Deposits 54 (5), 313–333.

Zhuravlev, A.Z., Zhuravlev, D.Z., Kostitsyn, Yu.A., Chernyshov, I.V., 1987. Determination of Sm/Nd ratio for geochronology. Geokhimiya 8, 1115–1129.

Editorial responsibility: A.E. Izokh